

Research Article

Stability of the Next-to-Tribimaximal Mixings under Radiative Corrections with the Variation of the SUSY Breaking Scale in MSSM

Kh. Helensana Devi ,¹ K. Sashikanta Singh ,¹ and N. Nimai Singh ,^{1,2}

¹Department of Physics, Manipur University, 795003 Imphal, India

²Research Institute of Science and Technology, 795003 Imphal, India

Correspondence should be addressed to Kh. Helensana Devi; helensanakhumanthem2@manipuruniv.ac.in

Received 1 March 2023; Revised 22 September 2023; Accepted 3 November 2023; Published 24 November 2023

Academic Editor: Theocharis Kosmas

Copyright © 2023 Kh. Helensana Devi et al. This is an open access article distributed under the Creative Commons Attribution License, which permits unrestricted use, distribution, and reproduction in any medium, provided the original work is properly cited. The publication of this article was funded by SCOPA³.

We analyze the radiative stability of the next-to-tribimaximal mixings (NTBM) with the variation of the SUSY breaking scale (m_S) in MSSM, for both normal ordering (NO) and inverted ordering (IO) at the fixed input value of the seesaw scale $M_R = 10^{15}$ GeV and two different values of $\tan \beta$. All the neutrino oscillation parameters receive varying radiative corrections irrespective of the m_S values at the electroweak scale, which are all within the 3σ range of the latest global fit data at a low value of $\tan \beta$. NO is found to be more stable than IO for all four different NTBM mixing patterns.

1. Introduction

Neutrino oscillations have been very well established by measuring the neutrino-mixing parameters θ_{12} , θ_{23} , θ_{13} , Δm_{21}^2 , and Δm_{31}^2 [1]. One of the promising candidates for explaining the observed Pontecorvo-Maki-Nakagawa-Sakata (PMNS) mixing matrix is the tribimaximal (TBM) [2] which is ruled out due to the discovery of the nonzero value of θ_{13} [3–9]. Hence, in order to accommodate $\theta_{13} \neq 0$, the PMNS matrix is reproduced using the next-to-TBM (NTBM) [10, 11] which predicts the correlations among the phase and mixing angles. Existence of the PMNS-mixing matrix, which is the analogue of the CKM matrix in the quark sector, is the consequence of diagonalisation of the neutrino mass matrix. The PMNS-mixing matrix contains three mixing angles θ_{12} , θ_{23} , and θ_{13} and a phase δ_{CP} responsible for CP violation. Two additional phases which do not influence neutrino oscillations are added if we consider neutrinos as Majorana fermions. The measurement of a nonzero θ_{13} using reactor neutrinos in 2012 has opened the possibility to measure CP violation in the lepton sector.

The present work is a continuation of our previous work [12] on neutrino masses and mixings with varying SUSY breaking scale m_S under RGEs [12–19]. We study both normal- and inverted-ordering neutrino mass models. We adopt the bottom-up approach for running gauge and Yukawa couplings from low to high energy scales and the top-down approach for running neutrino parameters from high to low energy scales, along with gauge and Yukawa couplings.

Following the discovery of a nonzero θ_{13} , the originally proposed TBM (tribimaximal) mixing pattern, which initially assumed θ_{13} to be zero, was no longer considered a valid description. Consequently, extensive research efforts were directed towards exploring various TBM variants capable of accommodating a nonzero θ_{13} while accurately reproducing the PMNS (Pontecorvo-Maki-Nakagawa-Sakata) matrix. Among these variants, the next-to-TBM- (NTBM-) mixing scheme has gained prominence. NTBM mixing is characterized by a two-parameter family and has played a crucial role in making precise predictions and establishing correlations among the mixing angles θ_{ij} and the Dirac CP

phase δ_{CP} . Multiple model-independent analyses have delved into these correlations, with references available in [10, 11, 20–22]. It is worth emphasizing that the original TBM-mixing pattern, denoted as V_{TBM} , explicitly predicts θ_{13} to be exactly zero. However, thorough global fit studies, as summarized in Table 1, have unequivocally demonstrated the existence of a nonzero θ_{13} . Consequently, a strong incentive exists to investigate deviations from the TBM-mixing pattern. Phenomenologically, small deviations from the TBM pattern can be easily parameterized by multiplication with a unitary rotation matrix. For example, the TBM_1 -mixing scheme, given in equation (2), can be seen as a modification to the TBM-mixing pattern by applying a 23-rotation matrix R_{23} from the right to V_{TBM} . In this sense, the rotation matrix $R_{23}(\kappa_1, \kappa_2)$ could also be interpreted as a perturbation to the exact TBM-mixing pattern. The physical observables—namely, the three mixing angles and the Dirac CP phase δ_{CP} —are correlated via the two parameters κ_1 and κ_2 , which leads us to a well-defined phenomenology.

There are four allowed NTBM patterns [23] depending on the position (left or right) of the multiplication by a unitary rotation matrix to tribimaximal (TBM) mixing. The V_{TBM} is given by

$$V_{TBM} = \begin{pmatrix} \sqrt{\frac{2}{3}} & \frac{1}{\sqrt{3}} & 0 \\ -\frac{1}{\sqrt{6}} & \frac{1}{\sqrt{3}} & \frac{1}{\sqrt{2}} \\ -\frac{1}{\sqrt{6}} & \frac{1}{\sqrt{3}} & -\frac{1}{\sqrt{2}} \end{pmatrix}. \quad (1)$$

The four allowed NTBM patterns are [23]

$$U_1 = V_{TBM} R_{23}, \quad (2)$$

$$U_2 = V_{TBM} R_{13}, \quad (3)$$

$$U^2 = R_{13} V_{TBM}, \quad (4)$$

$$U^3 = R_{12} V_{TBM}, \quad (5)$$

where R_{23} , R_{13} , and R_{12} are the rotation matrices defined as

$$\begin{aligned} R_{23} &= \begin{pmatrix} 1 & 0 & 0 \\ 0 & \cos \kappa_1 & \sin \kappa_1 e^{i\kappa_2} \\ 0 & -\sin \kappa_1 e^{-i\kappa_2} & \cos \kappa_1 \end{pmatrix}, \\ R_{13} &= \begin{pmatrix} \cos \kappa_1 & 0 & \sin \kappa_1 e^{i\kappa_2} \\ 0 & 1 & 0 \\ -\sin \kappa_1 e^{-i\kappa_2} & 0 & \cos \kappa_1 \end{pmatrix}, \\ R_{12} &= \begin{pmatrix} \cos \kappa_1 & \sin \kappa_1 e^{i\kappa_2} & 0 \\ -\sin \kappa_1 e^{-i\kappa_2} & \cos \kappa_1 & 0 \\ 0 & 0 & 1 \end{pmatrix}, \end{aligned} \quad (6)$$

where κ_1 and κ_2 are free parameters within the ranges $0 \leq \kappa_1 \leq \pi$ and $0 \leq \kappa_2 < 2\pi$, respectively. U_1 , U_2 , U^2 , and U^3 are distinct NTBM-mixing patterns for the TBM_1 , $TB M_2$, TBM^2 , and TBM^3 scenarios, respectively. In the present work, we calculate the values of mixing angles and δ_{CP} given by these four different mixing patterns, and these are found to be valid for certain values of κ_1 and κ_2 . We check the stability against radiative corrections by varying the SUSY breaking scale m_S within the range of 2–14 TeV, considering two different values of $\tan \beta = 30, 50$. The paper is organized as follows. NTBM is discussed in Section 2. Analysis for RGEs is discussed in Section 3. Numerical analysis and results are given in Section 4. Section 5 concludes the paper.

2. Numerical Predictions in Next-to-TBM (NTBM)

NTBM is defined by multiplying V_{TBM} by a unitary rotation matrix on either the left or the right. There are six possible NTBM patterns, but only four patterns given in equations (2)–(5) are allowed since two patterns: $U_P = V_{TBM} R_{12}$ and $U_P = R_{23} V_{TBM}$, are already excluded as they predict zero θ_{13} . The four NTBM patterns provide formulas for the mixing angles and δ_{CP} in terms of free parameters κ_1 and κ_2 , which characterize the two-parameter family of NTBM patterns [23]. The four patterns are given as follows.

2.1. TBM_1 Pattern.

$$\begin{aligned} \tan \theta_{23} &= \frac{|3\sqrt{2} \cos \kappa_1 + 2\sqrt{3}e^{i\kappa_2} \sin \kappa_1|}{|3\sqrt{2} \cos \kappa_1 - 2\sqrt{3}e^{i\kappa_2} \sin \kappa_1|}, \\ \tan \theta_{12} &= \frac{|\cos \kappa_1|}{\sqrt{2}}, \quad \sin \theta_{13} = \frac{|\sin \kappa_1|}{\sqrt{3}}, \\ \sin \delta_{CP} &= \frac{(\sin 2\kappa_1) \sin \kappa_2 (\cos 2\kappa_1 + 5)}{\left[(\cos \kappa_1 + 5)^2 - (2\sqrt{6} \sin 2\kappa_1 \cos \kappa_2)^2 \right]^{1/2}}. \end{aligned} \quad (7)$$

2.2. TBM_2 Pattern.

$$\begin{aligned} \tan \theta_{23} &= \frac{|\sqrt{3}e^{i\kappa_2} \sin \kappa_1 - 3 \cos \kappa_1|}{|3 \cos \kappa_1 + \sqrt{3}e^{i\kappa_2} \sin \kappa_1|}, \\ \tan \theta_{12} &= \frac{1}{\sqrt{2}|\cos \kappa_1|}, \\ \sin \theta_{13} &= \sqrt{\frac{2}{3}}|\sin \kappa_1|, \\ \sin \delta_{CP} &= \frac{(\sin 2\kappa_1)(\cos 2\kappa_1 + 2) \sin \kappa_2}{\left[(2 \cos^2 \kappa_1 + 1)^2 - 3 \sin^2 2\kappa_1 \cos^2 \kappa_2 \right]^{1/2}}. \end{aligned} \quad (8)$$

TABLE 1: Current best-fit values, 1σ errors, and 2σ and 3σ intervals for the neutrino oscillation parameters from global data which are adopted from References [1, 26, 27].

Parameters	Best fit	2σ	3σ
$\Delta m_{21}^2 [10^{-5} \text{ eV}^2]$	$7.50^{+0.22}_{-0.20}$	7.12–7.93	6.94–8.14
$\Delta m_{31}^2 [10^{-3} \text{ eV}^2]$ (NO)	$2.55^{+0.02}_{-0.03}$	2.49–2.60	2.47–2.63
$\Delta m_{31}^2 [10^{-3} \text{ eV}^2]$ (IO)	$2.45^{+0.02}_{-0.03}$	2.39–2.50	2.37–2.53
θ_{23} (NO)	49.26 ± 0.79	47.37–50.71	41.20–51.33
θ_{23} (IO)	$49.46^{+0.60}_{-0.97}$	47.35–50.67	41.16–51.25
θ_{12}	34.3 ± 1.0	32.3–36.4	31.4–37.4
θ_{13} (NO)	$8.53^{+0.13}_{-0.12}$	8.27–8.79	8.13–8.92
θ_{13} (IO)	$8.58^{+0.12}_{-0.14}$	8.30–8.83	8.17–8.96
δ_{CP} (NO)	194^{+24}_{-22}	152–255	128–359
δ_{CP} (IO)	284^{+26}_{-28}	226–332	200–353
$ \Sigma m_i $	<0.12 eV; ≥ 0.06 eV		

TABLE 2: The allowed input set of neutrino parameters at the high-energy scale $M_R = 10^{15}$ GeV and $\tan \beta = 30, 50$ encompasses four different patterns. $\theta_{23}, \theta_{12}, \theta_{13}$, and δ_{CP} are estimated values, while the others are arbitrary allowed input values. In this paper, we consider both the NO and IO.

ν		TBM ₁	TBM ₂	TBM ²	TBM ³
Input		$\kappa_1 = 2.8916$	$\kappa_1 = 2.958$	$\kappa_1 = 2.931593$	$\kappa_1 = 2.93$
Parameters		$\kappa_2 = 1.641592$	$\kappa_2 = 1.483182$	$\kappa_2 = 4.92477$	$\kappa_2 = 1.2832$
m_1 (eV)		0.012	0.012	0.012	0.012
m_2 (eV)		$1.245 \times m_1$	$1.245 \times m_1$	$1.245 \times m_1$	$1.245 \times m_1$
m_3 (eV)		$4.392 \times m_1$	$4.392 \times m_1$	$4.392 \times m_1$	$4.392 \times m_1$
$\theta_{12}/^0$	NO	34.416	35.7234	33.9229	33.2824
$\theta_{23}/^0$		45.8099	45.5314	45.6363	44.3539
$\theta_{13}/^0$		8.212	8.572	8.476	8.540
$\psi_1/^\circ$		0	0	0	0
$\psi_2/^\circ$		180	180	180	180
$\delta/^\circ$		208.581	200.957	203.939	203.864
ν		TBM ₁	TBM ₂	TBM ²	TBM ³
Input		$\kappa_1 = 0.25$	$\kappa_1 = 2.985$	$\kappa_1 = 0.21$	$\kappa_1 = 2.93$
Parameters		$\kappa_2 = 1.5$	$\kappa_2 = 4.8$	$\kappa_2 = 4.5$	$\kappa_2 = 5$
m_3 (eV)		0.009	0.009	0.009	0.009
m_1 (eV)		$5.661 \times m_3$	$5.661 \times m_3$	$5.661 \times m_3$	$5.661 \times m_3$
m_2 (eV)		$5.696 \times m_3$	$5.696 \times m_3$	$5.696 \times m_3$	$5.696 \times m_3$
$\theta_{12}/^0$		34.416	35.7234	33.9229	33.2824
$\theta_{23}/^0$	IO	45.8099	45.5314	45.6363	44.3539
$\theta_{13}/^0$		8.212	8.572	8.476	8.540
$\psi_1/^\circ$		0	0	0	0
$\psi_2/^\circ$		180	180	180	180
$\delta/^\circ$		208.582	200.957	203.939	203.87

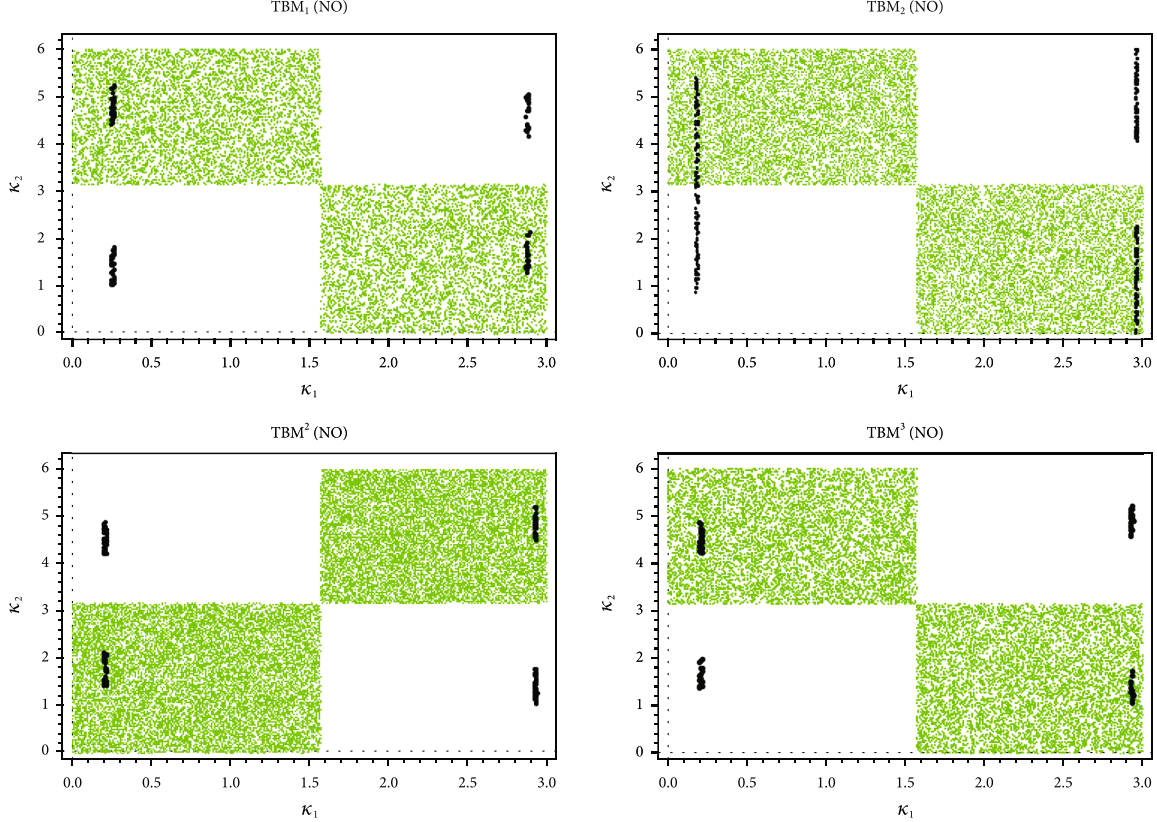


FIGURE 1: Constraints on the two free parameters κ_1 and κ_2 are applied in the context of the NO spectrum. The 3σ -allowed mixing angles are shaded in black, and regions where $\sin \delta_{CP} > 0$ are shaded in green, both for the four different mixing patterns of NTBM.

2.3. TBM² Pattern.

$$\begin{aligned} \tan \theta_{23} &= \frac{1}{|\cos \kappa_1|}, \quad \frac{\tan \theta_{12}}{\sqrt{2}} = \left| \frac{\cos \kappa_1 + e^{i\kappa_2} \sin \kappa_1}{2 \cos \kappa_1 - e^{i\kappa_2} \sin \kappa_1} \right|, \\ \sin \theta_{13} &= \frac{|\sin \kappa_1|}{\sqrt{2}}, \\ \sin \delta_{CP} &= \frac{(\sin 2\kappa_1)(\cos 2\kappa_1 + 3) \sin \kappa_2}{2[(-2 \sin 2\kappa_1 \cos \kappa_2 + 3 \cos^2 \kappa_1 + 1)(1 + \sin 2\kappa_1 \cos \kappa_2)]^{1/2}}. \end{aligned} \quad (9)$$

2.4. TBM³ Pattern.

$$\begin{aligned} \tan \theta_{23} &= |\cos \kappa_1|, \quad \frac{\tan \theta_{12}}{\sqrt{2}} = \left| \frac{\cos \kappa_1 + e^{i\kappa_2} \sin \kappa_1}{2 \cos \kappa_1 - e^{i\kappa_2} \sin \kappa_1} \right|, \\ \sin \theta_{13} &= \frac{|\sin \kappa_1|}{\sqrt{2}}, \\ \sin \delta_{CP} &= \frac{(\sin 2\kappa_1)(\cos 2\kappa_1 + 3) \sin \kappa_2}{2[(-2 \sin 2\kappa_1 \cos \kappa_2 + 3 \cos^2 \kappa_1 + 1)(1 + \sin 2\kappa_1 \cos \kappa_2)]^{1/2}}. \end{aligned} \quad (10)$$

We impose the conditions $\sin \delta_{CP} > 0$ (NO) and $\sin \delta_{CP} < 0$ (IO) to constrain the two free parameters κ_1 and κ_2 for all NTBM scenarios. The best-estimated numerical values of θ_{ij} and δ_{CP} for TBM₁, TBM₂, TBM², and TBM³ are provided in Table 2 for specific choices of κ_1 and κ_2 in each case, both for NO and IO. We use values of κ_1 and κ_2

that fall within the allowed regions depicted in Figures 1 and 2 for both NO and IO, respectively

3. Analysis for RGEs

Numerical analysis of Renormalization Group Equations (RGEs) [18, 24, 25] is conducted in two successive steps: first, bottom-up running, and second, top-down running. Two-loop Renormalization Group Equations (RGEs) for gauge and Yukawa couplings are provided in Appendix A for both the Standard Model (SM) and the Minimal Supersymmetric Standard Model (MSSM). The RGEs for neutrino oscillation parameters are presented in Appendix B.

3.1. Bottom-Up Running. Bottom-up running is used to extract the values of gauge and Yukawa couplings at a high energy scale using RGEs which can be divided into three regions, $m_Z < \mu < m_t$, $m_t < \mu < m_S$, and $m_S < \mu < M_R$. We use recent experimental data [1, 26] as initial input values at the low energy scale, which are given in Table 3.

We calculate the values of gauge couplings, α_2 for $SU(2)_L$, and α_1 for $U(1)_Y$, by using $\sin^2 \theta_W(m_Z) = \alpha_{em}(m_Z)/\alpha_2(m_Z)$ and matching condition,

$$\frac{1}{\alpha_{em}(m_Z)} = \frac{5}{3} \frac{1}{\alpha_1(m_Z)} + \frac{1}{\alpha_2(m_Z)}. \quad (11)$$

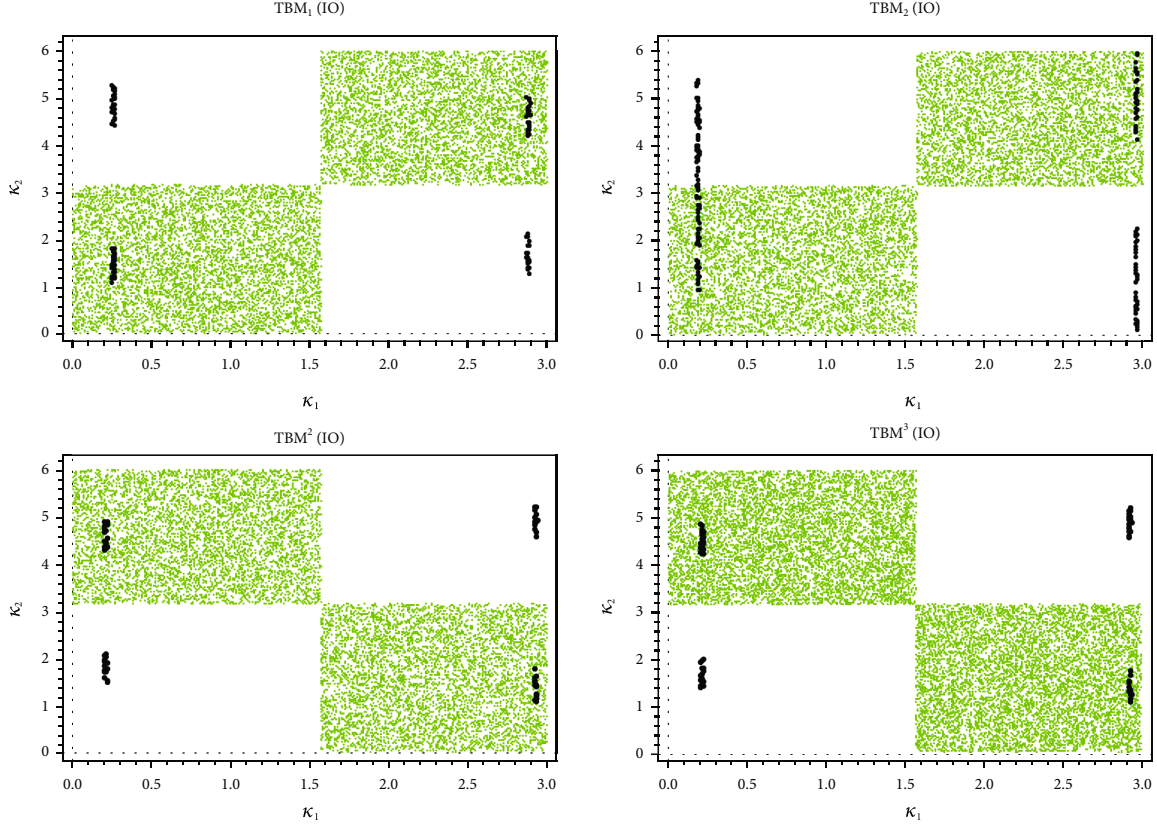


FIGURE 2: Constraints on the two free parameters κ_1 and κ_2 are imposed within the inverted-ordering (IO) spectrum. The 3σ -allowed mixing angles are shaded in black, while regions where $\sin \delta_{CP} < 0$ are shaded in green, for the four different mixing patterns of NTBM.

TABLE 3: Current experimental data for fermion masses, gauge coupling constants, and Weinberg mixing angle.

Mass (GeV)	Coupling constants	Weinberg mixing angle
$m_Z(m_Z) = 91.1876$	$\alpha_{em}^{-1}(m_Z) = 127.952 \pm 0.009$	$\sin^2 \theta_W(m_Z) = 0.23121 \pm 0.00017$
$m_t(m_t) = 172.76$	$\alpha_s(m_Z) = 0.11179 \pm 0.009$	
$m_b(m_b) = 4.18$		
$m_\tau(m_\tau) = 1.77$		

The normalised couplings [18], $g_i = \sqrt{4\pi\alpha_i}$, where α_i 's are the gauge couplings and $i = 1, 2, 3$ denote electromagnetic, weak, and strong couplings, respectively. One-loop gauge coupling RGEs [28] for the evolution from the m_Z scale to m_t scale, are given below:

$$\frac{1}{\alpha_i(\mu)} = \frac{1}{\alpha_i(m_Z)} - \frac{b_i}{2\pi} \ln \frac{\mu}{m_Z}, \quad (12)$$

where $m_Z \leq \mu \leq m_t$ and $b_i = (5.30, -0.50, -4.00)$ for the non-SUSY case. Using the QED-QCD rescaling factor η [29], fermion masses at the m_t scale are given by $m_b(m_t) = m_b(m_b)/\eta_b$ and $m_\tau(m_t) = m_\tau(m_\tau)/\eta_\tau$, where $\eta_b = 1.53$ and $\eta_\tau = 1.015$. The Yukawa couplings at the m_t scale are given by $h_t(m_t) = m_t(m_t)/v_0$, $h_b(m_t) = m_b(m_b)/v_0\eta_b$, and $h_\tau(m_\tau) = m_\tau(m_\tau)/v_0\eta_\tau$, where $v_0 = 174$ GeV is the vacuum expectation

TABLE 4: Numerical calculated values for fermion masses, Yukawa couplings, and gauge couplings at m_t scale.

Fermion masses	Yukawa couplings	Gauge couplings
$m_t(m_t) = 172.76$ GeV	$h_t(m_t) = 0.9928$	$g_1(m_t) = 0.4635$
$m_b(m_t) = 2.73$ GeV	$h_b(m_t) = 0.0157$	$g_2(m_t) = 0.6511$
$m_\tau(m_t) = 1.75$ GeV	$h_\tau(m_t) = 0.0100$	$g_3(m_t) = 1.1890$

value (VEV) of the SM Higgs field. The calculated numerical values for fermion masses, Yukawa couplings, and gauge couplings at the m_t scale are given in Table 4.

The evolution of gauge and Yukawa couplings for running from m_t to the M_R scale using RGEs is given in

TABLE 5: Yukawa and gauge couplings were evaluated at $M_R = 10^{15}$ GeV for $\tan \beta = 30$, considering different choices of the m_S scale.

m_S (TeV)	h_t	h_b	h_τ	g_1	g_2	g_3
2	0.5884	0.1917	0.2449	0.6591	0.7024	0.7357
4	0.5753	0.1912	0.2471	0.6548	0.6980	0.7328
6	0.5662	0.1908	0.2488	0.6514	0.6945	0.7305
8	0.5621	0.1907	0.2496	0.6498	0.6927	0.7293
10	0.5582	0.1906	0.2505	0.6481	0.6910	0.7282
12	0.5545	0.1904	0.2513	0.6464	0.6893	0.7271
14	0.5528	0.1903	0.2517	0.6456	0.6885	0.7265

TABLE 6: Yukawa and gauge couplings were evaluated at $M_R = 10^{15}$ GeV for $\tan \beta = 50$, considering different choices of the m_S scale.

m_S (TeV)	h_t	h_b	h_τ	g_1	g_2	g_3
2	0.6262	0.4097	0.5189	0.6587	0.7017	0.7353
4	0.6077	0.4012	0.5171	0.6544	0.6973	0.7324
6	0.5951	0.3954	0.5160	0.6511	0.6939	0.7301
8	0.5895	0.3927	0.5155	0.6494	0.6922	0.7290
10	0.5842	0.3902	0.5151	0.6477	0.6905	0.7279
12	0.5793	0.3878	0.5147	0.6461	0.6888	0.7268
14	0.5689	0.3819	0.5086	0.6453	0.7034	0.7263

Appendix A. The following matching conditions are applied at the transition point from SM ($m_t < \mu < m_S$) to MSSM ($m_S < \mu < M_R$) at the m_S scale, as

$$\left. \begin{array}{l} g_i(\text{SUSY}) = g_i(\text{SM}) \\ h_t(\text{SUSY}) = \frac{h_t(\text{SM})}{\sin \beta} = h_t(\text{SM}) \times \frac{\sqrt{1 + \tan^2 \beta}}{\tan \beta} \\ h_b(\text{SUSY}) = \frac{h_b(\text{SM})}{\cos \beta} = h_b(\text{SM}) \times \sqrt{1 + \tan^2 \beta} \\ h_\tau(\text{SUSY}) = \frac{h_\tau(\text{SM})}{\cos \beta} = h_\tau(\text{SM}) \times \sqrt{1 + \tan^2 \beta} \end{array} \right\}. \quad (13)$$

In the present work, we have observed the following trends at input values of $\tan \beta = 30$ and $\tan \beta = 50$. At $\tan \beta = 30$, both h_t and h_b decrease as the m_S scale increases, while h_τ increases with the increment in the m_S scale due to its dependence on $\tan \beta$, as demonstrated in equation (13). These trends are illustrated in Table 5, which will serve as input values for the subsequent top-down running at the high energy scale M_R . On the other hand, at $\tan \beta = 50$, all gauge and Yukawa couplings decrease with increasing m_S , as shown in Table 6.

3.2. Top-Down Running. We use the top-down running approach to study the stability for four patterns using RGEs against varying m_S at a fixed value of the seesaw scale $M_R = 10^{15}$ GeV and $\tan \beta = 30, 50$. In this running, we use the values of the Yukawa and gauge couplings which were earlier estimated at the M_R scale, as initial inputs. We consider simple mass relations for both NO and IO in order to minimize the number of input-free parameters, and both their sums of the

three neutrino mass eigenvalues $|\Sigma m_i|$ are all within the favorable range given by latest cosmological bound [30, 31]. We take the two Majorana phases ψ_1 and ψ_2 to be 0 and 180, respectively. We constraint the value of the Dirac CP phase δ_{CP} at 180°. Using all the necessary mathematical frameworks, we analyze the radiative nature of neutrino parameters like neutrino masses, mixings, and CP phases, using the top-down approach with the variations of the m_S scale at a fixed value of $\tan \beta$ for all allowed mixing patterns. In this work, we study the stability of TBM₁, TBM₂, TBM², and TBM³ considering the current experimental data given in Table 1. We assume a relation among the three neutrino mass eigenstates for all the four NTBM-mixing patterns. The values of the free parameters κ_1 and κ_2 are considered which satisfy the condition $\sin \delta_{CP} > 0$ for NO and $\sin \delta_{CP} < 0$ for IO. The input set at a high energy scale is given in Table 2.

4. Numerical Analysis and Results

Here, we analyze the impact of varying m_S while keeping the values of $M_R = 10^{15}$ GeV and $\tan \beta$ fixed at 30 and 50, respectively. We consider the effects on neutrino oscillation parameters for both NO and IO, presenting numerical data in Tables 7–10 and graphical representations in Figures 3 and 4.

At $\tan \beta = 30$, for NO, using the input set which is given in Table 2, it is found that all the neutrino oscillation parameters are in favor with the latest data which are within the 3σ range. All the three mixing angles decrease with increasing m_S , but Δm_{ij}^2 increases with increasing m_S . δ_{CP} almost maintains stability against the variation of m_S .

At $\tan \beta = 30$, for IO, using the input set which is given in Table 2, it is found that all the neutrino oscillation parameters are in favor with the latest data which are within the 3σ

TABLE 7: Effects on the output of θ_{ij} , Δm_{ij}^2 , and $|\Sigma m_i|$ at a low-energy scale, on varying m_S for four different NTBM patterns (NO) at $\tan \beta = 30$ and $M_R = 10^{15}$ GeV.

m_S (TeV)	$\theta_{23}/^0$				$\theta_{12}/^0$				$\theta_{13}/^0$			
	TBM ₁	TBM ₂	TBM ²	TBM ³	TBM ₁	TBM ₂	TBM ²	TBM ³	TBM ₁	TBM ₂	TBM ²	TBM ³
2	45.936	45.666	45.762	44.476	34.399	35.707	33.907	33.265	8.269	8.642	8.539	8.601
4	45.905	45.636	45.732	44.446	34.392	35.700	33.899	33.257	8.251	8.625	8.521	8.583
6	45.888	45.618	45.714	44.429	34.388	35.696	33.895	33.253	8.241	8.615	8.511	8.573
8	45.875	45.605	45.701	44.416	34.385	35.692	33.892	33.250	8.233	8.606	8.503	8.564
10	45.865	45.595	45.691	44.406	34.382	35.690	33.890	33.247	8.226	8.601	8.497	8.558
12	45.857	45.587	45.683	44.398	34.380	35.688	33.888	33.246	8.222	8.596	8.492	8.554
14	45.849	45.580	45.676	44.390	34.379	35.686	33.886	33.244	8.217	8.592	8.487	8.549
m_S (TeV)	Δm_{31}^2 (10^{-3} eV 2)				Δm_{21}^2 (10^{-5} eV 2)				$ \Sigma m_i $			
	TBM ₁	TBM ₂	TBM ²	TBM ³	TBM ₁	TBM ₂	TBM ²	TBM ³	TBM ₁	TBM ₂	TBM ²	TBM ³
2	2.4622	2.4626	2.4631	2.4611	7.650	7.688	7.652	7.663	0.0758	0.0758	0.0758	0.0758
4	2.4736	2.4747	2.4766	2.4730	7.709	7.751	7.712	7.725	0.0755	0.0756	0.0756	0.0756
6	2.4807	2.4817	2.4831	2.4802	7.755	7.788	7.759	7.772	0.0754	0.0755	0.0755	0.0755
8	2.4820	2.4829	2.4832	2.4816	7.756	7.798	7.760	7.773	0.0753	0.0754	0.0754	0.0754
10	2.4824	2.4834	2.4846	2.4814	7.762	7.806	7.766	7.781	0.0752	0.0753	0.0753	0.0753
12	2.4845	2.4853	2.4857	2.4820	7.772	7.818	7.776	7.791	0.0751	0.0752	0.0752	0.0752
14	2.4846	2.4864	2.4866	2.4842	7.774	7.819	7.780	7.792	0.0750	0.0751	0.0751	0.0751

TABLE 8: Effects on the output of θ_{ij} , Δm_{ij}^2 , and $|\Sigma m_i|$ at a low-energy scale, on varying m_S for four different NTBM patterns (NO) at $\tan \beta = 50$ and $M_R = 10^{15}$ GeV.

m_S (TeV)	$\theta_{23}/^0$				$\theta_{12}/^0$				$\theta_{13}/^0$			
	TBM ₁	TBM ₂	TBM ²	TBM ³	TBM ₁	TBM ₂	TBM ²	TBM ³	TBM ₁	TBM ₂	TBM ²	TBM ³
2	46.574	46.316	46.394	45.101	34.430	35.736	33.936	33.292	8.668	9.069	8.910	9.009
4	46.512	46.253	46.332	45.039	34.418	35.725	33.925	33.281	8.644	9.046	8.887	8.986
6	46.475	46.216	46.295	45.003	34.412	35.718	33.919	33.274	8.630	9.033	8.873	8.972
8	46.450	46.190	46.270	44.977	34.407	35.713	33.914	33.270	8.620	9.023	8.863	8.962
10	46.430	46.170	46.250	44.958	34.403	35.710	33.910	33.266	8.612	9.015	8.855	8.954
12	46.414	46.155	46.235	44.942	34.400	35.707	33.907	33.263	8.606	9.009	8.849	8.948
14	46.386	46.126	46.206	44.914	34.396	35.703	33.903	33.259	8.591	8.993	8.834	8.933
m_S (TeV)	Δm_{31}^2 (10^{-3} eV 2)				Δm_{21}^2 (10^{-5} eV 2)				$ \Sigma m_i $			
	TBM ₁	TBM ₂	TBM ²	TBM ³	TBM ₁	TBM ₂	TBM ²	TBM ³	TBM ₁	TBM ₂	TBM ²	TBM ³
2	2.018	2.019	2.020	2.015	6.602	6.697	6.607	6.629	0.0688	0.0685	0.0686	0.0688
4	2.033	2.034	2.035	2.030	6.675	6.769	6.681	6.705	0.0687	0.0687	0.0687	0.0686
6	2.047	2.048	2.049	2.044	6.732	6.826	6.737	6.764	0.0687	0.0687	0.0687	0.0686
8	2.044	2.045	2.046	2.041	6.728	6.822	6.734	6.762	0.0684	0.0684	0.0684	0.0683
10	2.045	2.046	2.047	2.042	6.736	6.829	6.742	6.770	0.0683	0.0683	0.0683	0.0683
12	2.048	2.049	2.051	2.046	6.751	6.843	6.757	6.785	0.0683	0.0683	0.0683	0.0683
14	2.051	2.052	2.054	2.049	7.047	7.143	7.054	7.084	0.0682	0.0682	0.0682	0.0682

range. All the three mixing angles and δ_{CP} maintain more stability as compared to Δm_{ij}^2 . Both θ_{23} and θ_{13} increase but θ_{12} decreases against the variation of m_S . Δm_{21}^2 increases whereas Δm_{31}^2 decreases with increasing m_S , and Δm_{31}^2 main-

tains more stability as compared to Δm_{21}^2 at higher m_S . It is observed from Tables 7 and 9 and their graphical representations in Figures 3 and 5 that NO maintains more stability than the IO.

TABLE 9: Effects on the output of θ_{ij} , $|\Delta m_{ij}^2|$, and $|\Sigma m_i|$ at a low-energy scale, on varying m_S for four different NTBM patterns (IO) at $\tan \beta = 30$ and $M_R = 10^{15}$ GeV.

m_S (TeV)	$\theta_{23}/^0$				$\theta_{12}/^0$				$\theta_{13}/^0$			
	TBM ₁	TBM ₂	TBM ²	TBM ³	TBM ₁	TBM ₂	TBM ²	TBM ³	TBM ₁	TBM ₂	TBM ²	TBM ³
2	45.8174	44.5423	45.6469	44.3643	34.375	35.684	33.882	33.242	8.2114	8.5720	8.4762	8.5400
4	45.8240	44.5490	45.6535	44.3708	34.367	35.676	33.875	33.235	8.2128	8.5737	8.4778	8.5415
6	45.8283	44.5533	45.6577	44.3749	34.363	35.671	33.870	33.230	8.2139	8.5748	8.4789	8.5426
8	45.8311	44.5563	45.6605	44.3778	34.360	35.668	33.867	33.227	8.2145	8.5756	8.4796	8.5433
10	45.8334	44.5585	45.6627	44.3802	34.357	35.666	33.865	33.225	8.2151	8.5763	8.4802	8.5439
12	45.8355	44.5607	45.6648	44.3819	34.355	35.664	33.863	33.223	8.2156	8.5768	8.4807	8.5444
14	45.8371	44.5624	45.6664	44.3835	34.353	35.662	33.861	33.221	8.2160	8.5773	8.4811	8.5448
m_S (TeV)	$ \Delta m_{31}^2 (10^{-3} \text{ eV}^2)$				$ \Delta m_{21}^2 (10^{-5} \text{ eV}^2)$				$ \Sigma m_i $			
	TBM ₁	TBM ₂	TBM ²	TBM ³	TBM ₁	TBM ₂	TBM ²	TBM ³	TBM ₁	TBM ₂	TBM ²	TBM ³
2	2.457	2.459	2.458	2.458	6.489	6.658	6.499	6.559	0.1096	0.1096	0.1096	0.1096
4	2.431	2.433	2.431	2.432	7.146	7.346	7.158	7.230	0.1091	0.1091	0.1091	0.1091
6	2.416	2.418	2.416	2.417	7.489	7.707	7.501	7.581	0.1089	0.1089	0.1089	0.1089
8	2.405	2.407	2.405	2.406	7.764	7.996	7.778	7.864	0.1086	0.1087	0.1086	0.1086
10	2.396	2.399	2.396	2.398	7.957	8.197	7.970	8.059	0.1085	0.1085	0.1085	0.1085
12	2.390	2.392	2.390	2.391	8.099	8.348	8.113	8.206	0.1084	0.1084	0.1084	0.1084
14	2.383	2.385	2.383	2.384	8.257	8.512	8.272	8.366	0.1082	0.1083	0.1082	0.1083

TABLE 10: Effects on the output of θ_{ij} , $|\Delta m_{ij}^2|$, and $|\Sigma m_i|$ at a low-energy scale, on varying m_S for four different NTBM patterns (IO) at $\tan \beta = 50$ and $M_R = 10^{15}$ GeV.

m_S (TeV)	$\theta_{23}/^0$				$\theta_{12}/^0$				$\theta_{13}/^0$			
	TBM ₁	TBM ₂	TBM ²	TBM ³	TBM ₁	TBM ₂	TBM ²	TBM ³	TBM ₁	TBM ₂	TBM ²	TBM ³
2	45.762	45.481	45.590	44.307	34.339	35.646	33.847	33.206	8.190	8.550	8.453	8.522
4	45.791	45.511	45.619	44.335	34.326	35.632	33.833	33.192	8.200	8.561	8.463	8.532
6	45.808	45.528	45.635	44.352	34.318	35.624	33.825	33.184	8.206	8.568	8.470	8.538
8	45.819	45.540	45.647	44.363	34.312	35.619	33.820	33.179	8.210	8.573	8.474	8.542
10	45.828	45.549	45.656	44.372	34.308	35.615	33.816	33.175	8.213	8.577	8.478	8.546
12	45.836	45.556	45.663	44.380	34.305	35.611	33.813	33.171	8.216	8.580	8.481	8.549
14	45.842	45.564	45.670	44.386	34.303	35.610	33.811	33.170	8.219	8.582	8.483	8.551
m_S (TeV)	$ \Delta m_{31}^2 (10^{-3} \text{ eV}^2)$				$ \Delta m_{21}^2 (10^{-5} \text{ eV}^2)$				$ \Sigma m_i $			
	TBM ₁	TBM ₂	TBM ²	TBM ³	TBM ₁	TBM ₂	TBM ²	TBM ³	TBM ₁	TBM ₂	TBM ²	TBM ³
2	2.345	2.348	2.347	2.349	12.62	13.04	12.64	12.67	0.1084	0.1085	0.1084	0.1084
4	2.303	2.305	2.304	2.306	14.15	14.59	14.17	14.21	0.1078	0.1079	0.1079	0.1079
6	2.281	2.283	2.282	2.284	14.90	15.36	14.92	14.97	0.1076	0.1077	0.1076	0.1076
8	2.261	2.264	2.262	2.265	15.48	15.96	15.50	15.56	0.1074	0.1075	0.1074	0.1074
10	2.246	2.250	2.249	2.251	15.89	16.37	15.91	15.97	0.1072	0.1073	0.1072	0.1072
12	2.236	2.240	2.239	2.241	16.01	16.61	16.21	16.23	0.1071	0.1072	0.1071	0.1071
14	2.231	2.239	2.235	2.237	16.06	16.65	16.28	16.31	0.1070	0.1071	0.1070	0.1077

At $\tan \beta = 50$ and $M_R = 10^{15}$ GeV, the low energy values of the three mixing angles and δ_{CP} remain stable with the variation of m_S , for both the NO and IO scenarios. However, the low energy values of the Δm_{21}^2 with the variation of m_S are outside the range provided by the global fit data for IO,

but for NO, both the low energy values of the two-mass squared differences are within the global fit data, indicating slight preference of NO to IO. These results are presented in Tables 8 and 10 and are graphically represented in Figures 4 and 6.

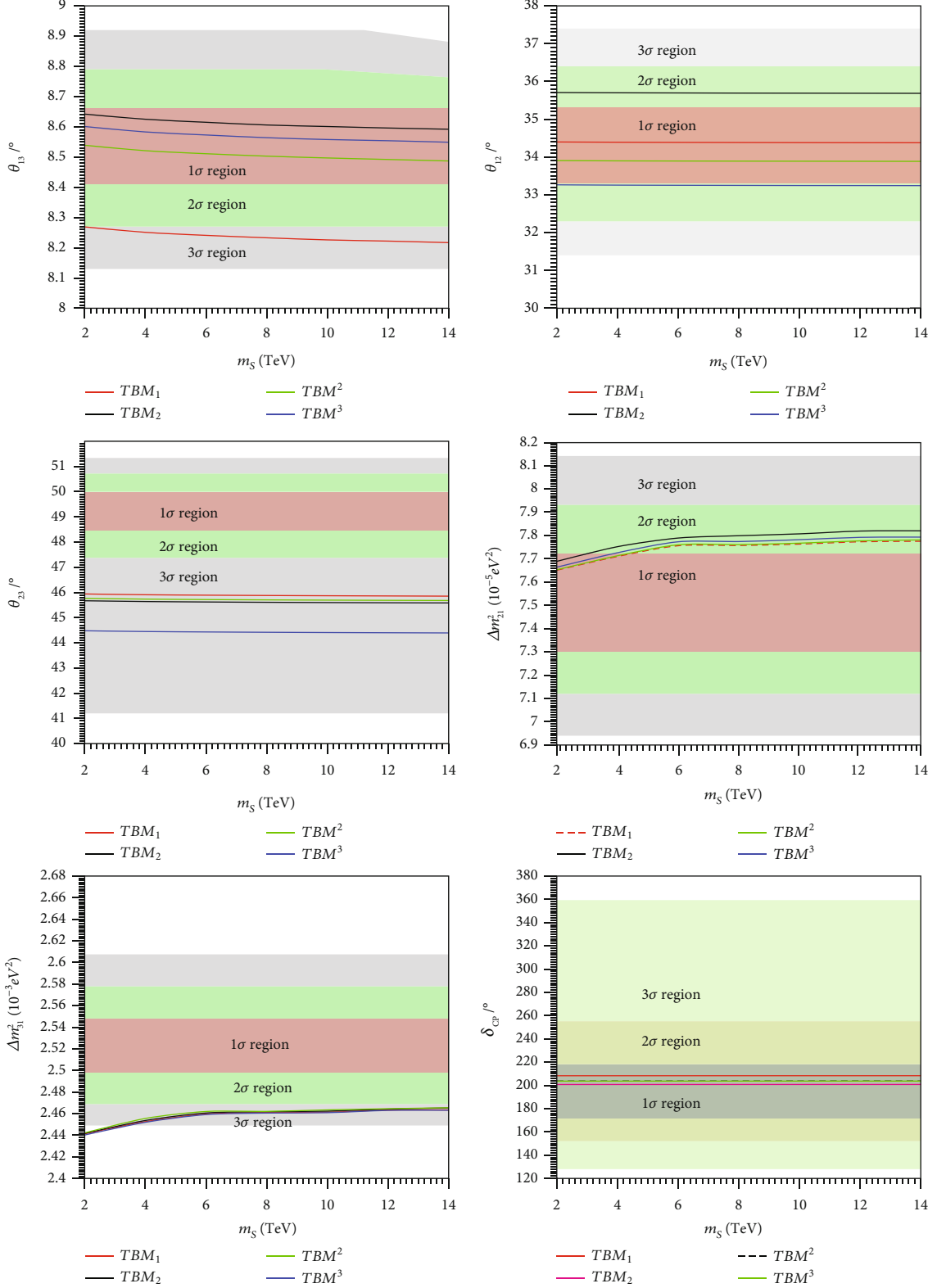


FIGURE 3: The variation of m_S for different NTBM patterns at $M_R = 10^{15}$ GeV and $\tan \beta = 30$ for NO leads to effects on the low-energy output results of θ_{ij} , $|\Delta m_{ij}^2|$, and δ_{CP} .

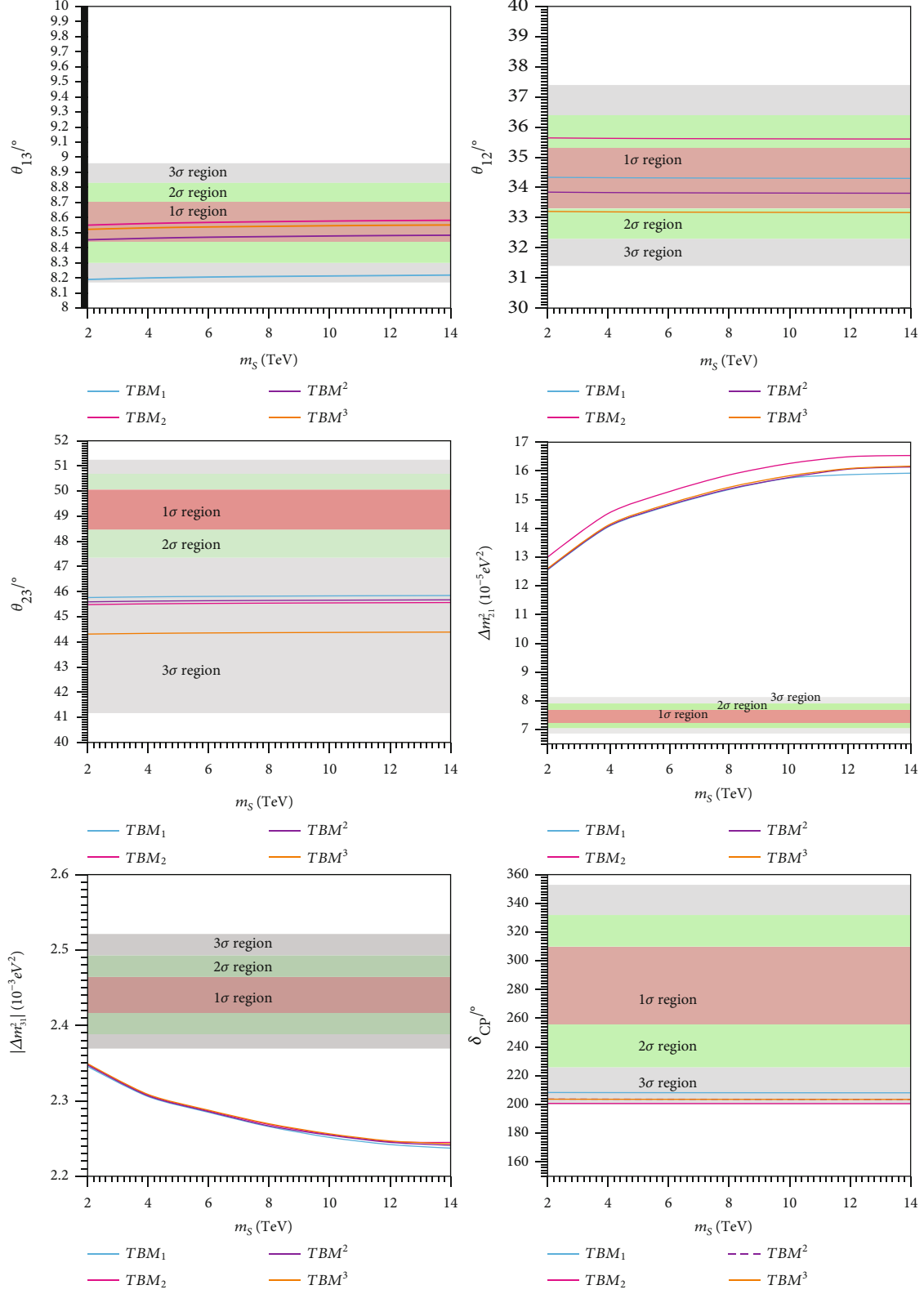


FIGURE 4: The variation of m_S for different NTBM patterns at $M_R = 10^{15}$ GeV and $\tan \beta = 50$ for IO leads to effects on the low-energy output results of θ_{ij} , $|\Delta m_{ij}^2|$, and δ_{CP} .

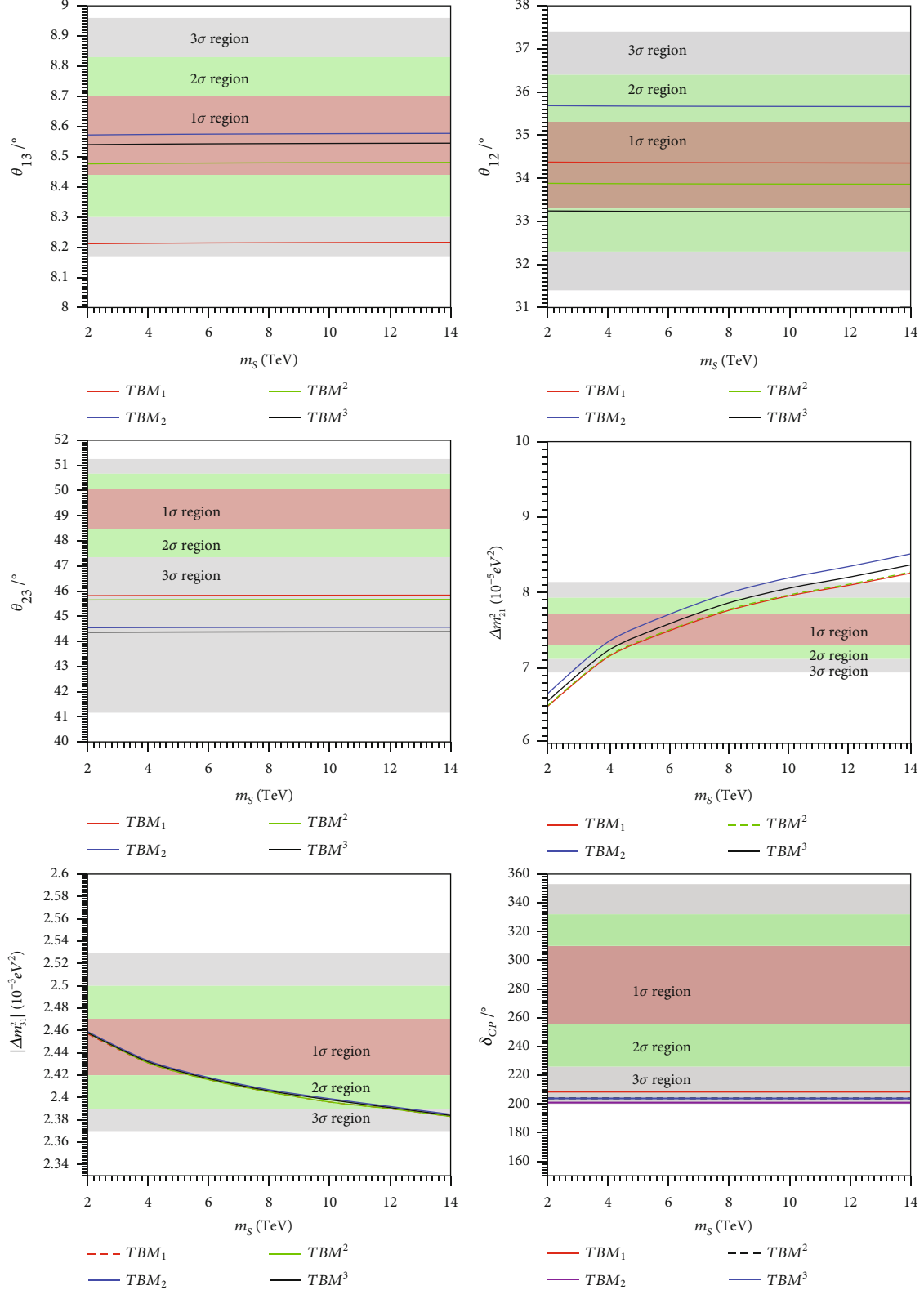


FIGURE 5: The variation of m_S for different NTBM patterns at $M_R = 10^{15}$ GeV and $\tan \beta = 30$ for IO leads to effects on the low-energy output results of θ_{ij} , $|\Delta m_{ij}^2|$, and δ_{CP} .

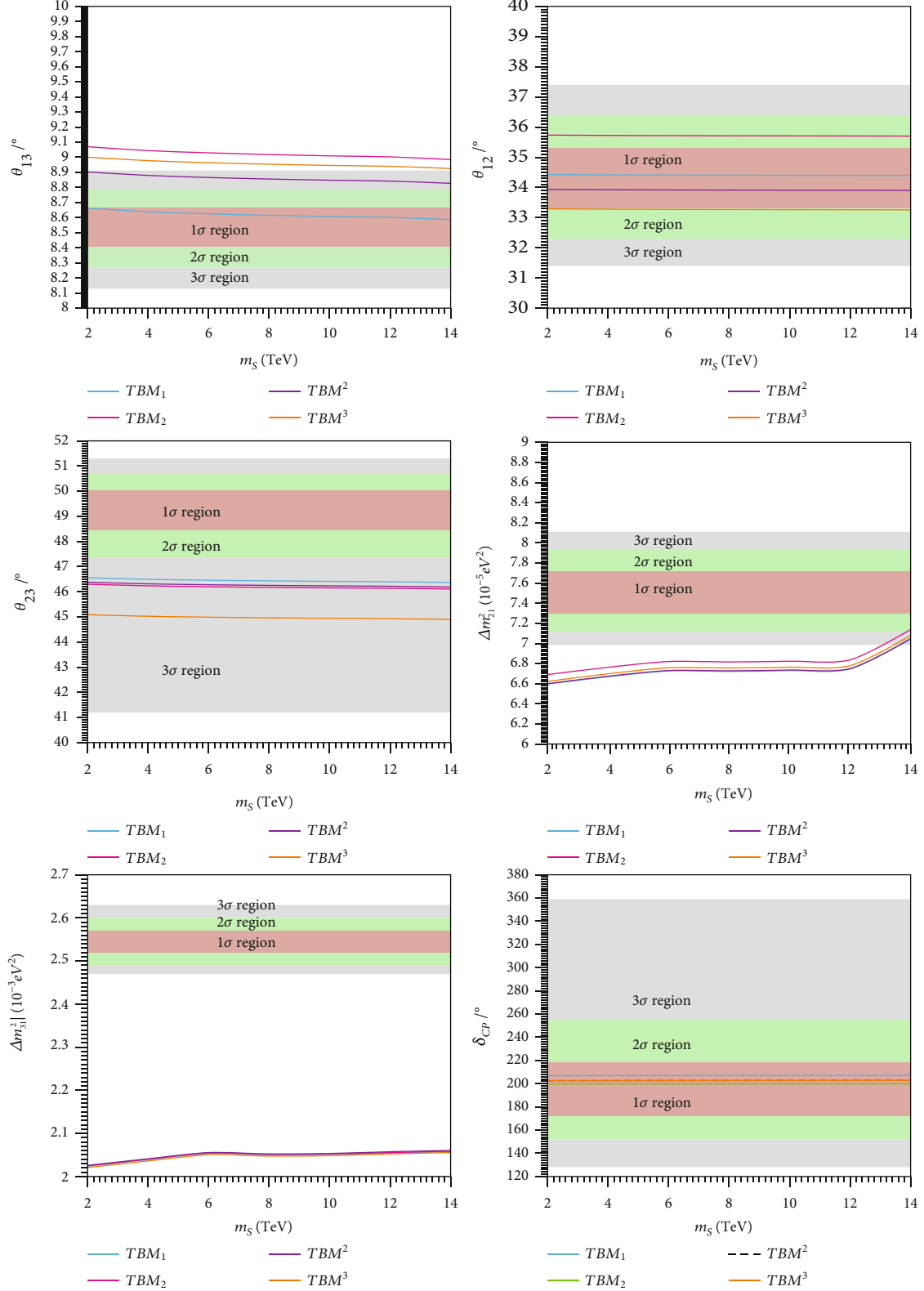


FIGURE 6: The variation of m_S for different NTBM patterns at $M_R = 10^{15}$ GeV and $\tan \beta = 50$ for NO leads to effects on the low-energy output results of θ_{ij} , $|\Delta m_{ij}^2|$, and δ_{CP} .

If we consider the position (left or right) of the multiplication by a unitary rotation matrix to tribimaximal (TBM) mixing, assuming these unitary rotation matrices are originated from charged lepton mass matrices, TBM² and TBM³ are acceptable as compared to TBM₁ and TBM₂, as the position of the unitary matrices should be on the left side of the TBM matrix. For example, $U^3 = R_{12} V_{\text{TBM}}$. Further, if we also consider the graphical analysis of κ_1 and κ_2 for obtaining the best fit in both NO and IO, TBM³ seems to be better than the other three types of NTBM, as the ranges of κ_1 and κ_2 in TBM³ are common for both NO and IO as shown in Figures 1 and 2 for four different NTBM patterns. For the other remaining three cases of NTBM, the ranges of κ_1 and κ_2 are different in NO and IO. Considering the above two points, our analysis shows that TBM³ is the best candidate.

5. Discussion and Conclusions

To summarize, we impose the following conditions to obtain the best fit pattern models among the NTBM.

The input of the sum of three neutrino masses should satisfy the latest PLANCK cosmological data $\Sigma|m_i| < 0.12 \text{ eV}$.

- (i) We apply the conditions $\sin \delta_{CP} > 0$ (NO) and $\sin \delta_{CP} < 0$ (IO) in order to constraint the two free parameters κ_1 and κ_2 , respectively, for all the NTBM scenarios
- (ii) We take the values of κ_1 and κ_2 which give the latest values of three mixing angles given by the latest global fit data
- (iii) We take different values of κ_1 and κ_2 which lie within the allowed regions as depicted in Figures 1 and 2 for four different NTBM patterns for both NO and IO

We study the stability for four different NTBM patterns at a fixed value of $M_R = 10^{15} \text{ GeV}$ and two different values of $\tan \beta$ (30, 50) for both NO and IO.

Case A ($\tan \beta = 30$): for NO, we have studied the stability for four patterns of NTBM using RGEs against the variation of m_S . There is a mile decrease of the mixing angles θ_{ij} and δ_{CP} with the increase of m_S (2 TeV–14 TeV). These are found to lie within 3σ ranges of observational data. Δm_{ij}^2 and δ_{CP} increase with increasing m_S . The low energy values of Δm_{21}^2 are found to lie within 2σ whereas those of Δm_{31}^2 lie within 3σ except for low values of m_S .

Similarly, for IO, the low energy values of Δm_{31}^2 and δ_{CP} decrease with the increase of m_S (2 TeV–14 TeV) which are found to lie within 3σ ranges. Δm_{21}^2 is found to lie within 3σ ranges, which increases with increasing m_S . θ_{ij} (except θ_{12}) increases slightly with the increase of m_S .

In short, it is found that NTBM-mixing patterns maintain stability under radiative corrections with the variation of m_S for a normal ordering case at the fixed value of seesaw scale M_R . All the neutrino oscillation parameters receive varying radiative corrections irrespective of the m_S values at the electroweak scale, which are all within the 3σ range

of the latest global fit data. NO maintains more stability as compared to IO with increasing m_S . All the four patterns of NTBM are found to be stable with the variation of m_S under radiative corrections in MSSM for both NO ($\sin \delta > 0$) and IO ($\sin \delta < 0$). If we consider the graphical analysis for κ_1 and κ_2 both for NO and IO as depicted in Figures 1 and 2, TBM³ is the best candidate, since it the most consistent one among the four NTBM cases.

Case B ($\tan \beta = 50$): for both NO and IO, the low energy values of all the three mixing angles with the variation of m_S are within the 3σ range. They remain stable with the variation of m_S . For IO, the low energy values of the Δm_{21}^2 with the variation of m_S fall outside the range of the global fit data. However, for NO, both the low energy values of the two-mass squared differences fall within the 3σ range of the global fit data. This indicates the slight preference for NO to IO in our numerical analysis. Additionally, all of the low energy values of the neutrino oscillation parameters undergo distinct radiative corrections. The graphical representations can be seen in Figures 4 and 6, accompanied by the numerical data presented in Tables 8 and 10.

Appendix

A. RGEs for Gauge Couplings [24]

The two-loop RGEs for gauge couplings are given by

$$\frac{dg_i}{dt} = \frac{b_i}{16\pi^2} g_i^3 + \frac{1}{(16\pi^2)^2} \left[\sum_{j=1}^3 b_{ij} g_i^3 g_j^2 - \sum_{j=t,b,\tau} a_{ij} g_i^3 h_j^2 \right], \quad (\text{A.1})$$

where $t = \ln \mu$ and b_i, b_{ij}, a_{ij} are β function coefficients in MSSM,

$$b_i = (6.6, \quad 1.0, \quad -3.0), \quad b_{ij} = \begin{pmatrix} 7.96 & 5.40 & 17.60 \\ 1.80 & 25.00 & 24.00 \\ 2.20 & 9.00 & 14.00 \end{pmatrix},$$

$$a_{ij} = \begin{pmatrix} 5.2 & 2.8 & 3.6 \\ 6.0 & 6.0 & 2.0 \\ 4.0 & 4.0 & 0.0 \end{pmatrix}, \quad (\text{A.2})$$

and, for the non-supersymmetric case, we have

$$b_i = (4.100, \quad -3.167, \quad -7.00), \quad b_{ij} = \begin{pmatrix} 3.98 & 2.70 & 8.8 \\ 0.90 & 5.83 & 12.0 \\ 1.10 & 4.50 & -26.0 \end{pmatrix},$$

$$a_{ij} = \begin{pmatrix} 0.85 & 0.5 & 0.5 \\ 1.50 & 1.5 & 0.5 \\ 2.00 & 2.0 & 0.0 \end{pmatrix}. \quad (\text{A.3})$$

A.1. Two-Loop RGEs for Yukawa Couplings and Quartic Higgs Coupling [24]. For MSSM,

$$\begin{aligned}
\frac{dh_t}{dt} &= \frac{h_t}{16\pi^2} \left(6h_t^2 + h_b^2 - \sum_{i=1}^3 c_i g_i^2 \right) \\
&\quad + \frac{h_t}{(16\pi^2)^2} \left[\sum_{i=1} \left(c_i b_i + \frac{c'_i}{2} \right) g_i^4 + g_1^2 g_2^2 \right. \\
&\quad + \frac{136}{45} g_1^2 g_3^2 + 8g_2^2 g_3^2 + \left(\frac{6}{5} g_1^2 + 6g_2^2 + 16g_3^2 \right) h_t^2 \\
&\quad + \frac{2}{5} g_1^2 h_b^2 - 22h_t^4 \\
&\quad \left. - 5h_b^4 - 5h_t^2 h_b^2 - h_b^2 h_\tau^2 \right], \\
\frac{dh_b}{dt} &= \frac{h_b}{16\pi^2} \left(6h_b^2 + h_\tau^2 + h_t^2 - \sum_{i=1}^3 c'_i g_i^2 \right) \\
&\quad + \frac{h_b}{(16\pi^2)^2} \left[\sum_{i=1} \left(c'_i b_i + \frac{c''_i}{2} \right) g_i^4 + g_1^2 g_2^2 + \frac{8}{9} g_1^2 g_3^2 \right. \\
&\quad + 8g_2^2 g_3^2 + \left(\frac{2}{5} g_1^2 + 6g_2^2 + 16g_3^2 \right) h_b^2 + \frac{4}{5} g_1^2 h_t^2 \\
&\quad + \frac{6}{5} g_1^2 h_\tau^2 - 22h_b^4 - 3h_\tau^4 - 5h_t^4 - 5h_b^2 h_t^2 - 3h_b^2 h_\tau^2 \left. \right], \\
\frac{dh_\tau}{dt} &= \frac{h_\tau}{16\pi^2} \left(4h_\tau^2 + 3h_b^2 - \sum_{i=1}^3 c''_i g_i^2 \right) \\
&\quad + \frac{h_\tau}{(16\pi^2)^2} \left[\sum_{i=1} \left(c''_i b_i + \frac{c'''_i}{2} \right) g_i^4 \right. \\
&\quad + \frac{9}{5} g_1^2 g_2^2 + \left(\frac{6}{5} g_1^2 + 6g_2^2 \right) h_\tau^2 \\
&\quad + \left(\frac{-2}{5} g_1^2 + 16g_3^2 \right) h_b^2 + 9h_b^4 - 10h_\tau^4 \\
&\quad \left. - 3h_b^2 h_t^2 - 9h_b^2 h_\tau^2 \right], \tag{A.4}
\end{aligned}$$

where

$$\begin{aligned}
c_i &= \left(\frac{13}{15}, 3, \frac{16}{13} \right), c'_i = \left(\frac{7}{15}, 3, \frac{16}{3} \right), \\
c''_i &= \left(\frac{9}{5}, 3, 0 \right). \tag{A.5}
\end{aligned}$$

For the non-supersymmetric case,

$$\begin{aligned}
\frac{dh_t}{dt} &= \frac{h_t}{16\pi^2} \left(\frac{3}{2} h_t^2 - \frac{3}{2} h_b^2 + Y_2(S) - \sum_{i=1}^3 c_i g_i^2 \right) \\
&\quad + \frac{h_t}{(16\pi^2)^2} \left[\left(\frac{1187}{600} \right) g_1^4 - \frac{23}{4} g_2^4 \right. \\
&\quad - 108g_3^4 - \frac{9}{20} g_1^2 g_2^2 + \frac{19}{15} g_1^2 g_3^2 + 9g_3^2 g_2^2 \\
&\quad + \left(\frac{223}{80} g_1^2 + \frac{135}{16} g_2^2 + 16g_3^2 \right) h_t^2 \\
&\quad - \left(\frac{43}{80} g_1^2 - \frac{9}{16} g_2^2 + 16g_3^2 \right) h_b^2 + \frac{5}{2} Y_4(S) \\
&\quad - 2\lambda(3h_t^2 + h_b^2) + \frac{3}{2} h_t^4 - \frac{5}{4} h_t^2 h_b^2 + \frac{11}{4} h_b^4 \\
&\quad \left. + Y_2(S) \left(\frac{5}{4} h_b^2 - \frac{9}{4} h_t^2 \right) - \eta_4(S) + \frac{3}{2} \lambda^2 \right], \\
\frac{dh_b}{dt} &= \frac{h_b}{16\pi^2} \left(\frac{3}{2} h_b^2 - \frac{3}{2} h_t^2 + Y_2(S) - \sum_{i=1}^3 c'_i g_i^2 \right) \\
&\quad + \frac{h_b}{(16\pi^2)^2} \left[-\frac{127}{600} g_1^4 - \frac{23}{4} g_2^4 \right. \\
&\quad - 108g_3^4 - \frac{27}{20} g_1^2 g_2^2 + \frac{31}{15} g_1^2 g_3^2 + 9g_3^2 g_2^2 \\
&\quad - \left(\frac{79}{80} g_1^2 - \frac{9}{16} g_2^2 + 16g_3^2 \right) h_t^2 \\
&\quad + \left(\frac{187}{80} g_1^2 + \frac{135}{16} g_2^2 + 16g_3^2 \right) h_b^2 + \frac{5}{2} Y_4(S) \\
&\quad - 2\lambda(3h_t^2 + 3h_b^2) + \frac{3}{2} h_b^4 - \frac{5}{4} h_t^2 h_b^2 + \frac{11}{4} h_t^4 \\
&\quad + Y_2(S) \left(\frac{5}{4} h_t^2 - \frac{9}{4} h_b^2 \right) - \eta_4(S) + \frac{3}{2} \lambda^2 \left. \right], \\
\frac{dh_\tau}{dt} &= \frac{h_\tau}{16\pi^2} \left(\frac{3}{2} h_\tau^2 + Y_2(S) - \sum_{i=1}^3 c''_i g_i^2 \right) \\
&\quad + \frac{h_\tau}{(16\pi^2)^2} \left[\frac{1371}{200} g_1^4 - \frac{23}{4} g_2^4 \right. \\
&\quad - \frac{27}{20} g_1^2 g_2^2 + \left(\frac{387}{80} g_1^2 + \frac{135}{16} g_2^2 \right) h_\tau^2 \\
&\quad + \frac{5}{2} Y_4(S) - 6\lambda h_t^2 + \frac{3}{2} h_\tau^4 \\
&\quad \left. - \frac{9}{4} Y_2(S) h_\tau^2 - \eta_4(S) + \frac{3}{2} \lambda^2 \right],
\end{aligned}$$

$$\begin{aligned}
\frac{d\lambda}{dt} = & \frac{1}{16\pi^2} \left[\frac{9}{4} \left(\frac{3}{25} g_1^4 + \frac{2}{5} g_2^2 g_1^2 + g_2^4 \right) - \left(\frac{9}{5} g_1^2 + 9 g_2^2 \right) \lambda \right. \\
& + 4 Y_2(S) \lambda - 4 H(S) + 12 \lambda^2 \Big] \\
& + \frac{1}{(16\pi^2)^2} \left[-78 \lambda^3 + 18 \left(\frac{3}{5} g_1^2 + 3 g_2^2 \right) \lambda^2 \right. \\
& + \left(-\frac{73}{8} g_2^4 + \frac{117}{20} g_1^2 g_2^2 + \frac{1887}{200} g_1^4 \right) \lambda \\
& + \frac{305}{8} g_2^6 - \frac{867}{120} g_1^2 g_2^4 - \frac{1677}{200} g_1^4 g_2^2 - \frac{3411}{1000} g_1^6 \\
& - 64 g_3^2 (h_t^4 + h_b^4) - \frac{8}{5} g_1^2 (2h_t^4 - h_b^4 + 3h_\tau^4) \\
& - \frac{3}{2} g_2^4 Y_2(S) + 10 \lambda Y_4(S) + \frac{3}{5} g_1^2 \left(-\frac{57}{10} g_1^2 + 21 g_2^2 \right) h_t^2 \\
& + \left(\frac{3}{2} g_1^2 + 9 g_2^2 \right) h_b^2 + \left(-\frac{15}{2} g_1^2 + 11 g_2^2 \right) h_\tau^2 \\
& - 24 \lambda^2 Y_2(S) - \lambda H(S) + 6 \lambda h_t^2 h_b^2 + 20 \left(3h_t^6 + 3h_b^6 + h_\tau^6 \right) \\
& \left. - 12 (h_t^4 h_b^2 + h_t^2 h_b^4) \right], \tag{A.6}
\end{aligned}$$

where

$$\begin{aligned}
Y_2(S) &= 3h_t^2 + 3h_b^2 + h_\tau^2, \\
Y_4(S) &= \frac{1}{3} \left[3\Sigma c_i g_i^2 h_t^2 + 3\Sigma c'_i g_i^2 h_b^2 + 3\Sigma c''_i g_i^2 h_\tau^2 \right], \\
H(S) &= 3h_t^4 + 3h_b^4 + h_\tau^4, \\
\eta_4(S) &= \frac{9}{4} \left[3h_t^4 + 3h_b^4 + h_\tau^4 - \frac{2}{3} h_t^2 h_b^2 \right], \tag{A.7}
\end{aligned}$$

and $\lambda = m_h^2/v_0^2$ is the Higgs self-coupling, $m_h = 125.78 \pm 0.26$ GeV is the Higgs mass [32], and $v_0 = 174$ GeV is the vacuum expectation value.

The beta function coefficients for non-SUSY case are given as follows: $c_i = (0.85, 2.25, 8.00)$, $c'_i = (0.25, 2.25, 8.00)$, and $c''_i = (2.25, 2.25, 0.00)$.

B. RGEs for Three Neutrino-Mixing Angles and Phases [33]: Neglecting Higher Order of θ_{13}

$$\begin{aligned}
\dot{\theta}_{12} &= -\frac{Ch_\tau^2}{32\pi^2} \sin 2\theta_{12} s_{23}^2 \frac{|m_1 e^{i\psi_1} + m_2 e^{i\psi_2}|^2}{\Delta m_{21}^2}, \\
\dot{\theta}_{13} &= \frac{Ch_\tau^2}{32\pi^2} \sin 2\theta_{12} \sin 2\theta_{23} \frac{m_3}{\Delta m_{31}^2 (1 + \xi)} \\
&\times [m_1 \cos(\psi_1 - \delta) - (1 + \xi)m_2 \cos(\psi_2 - \delta) - \xi m_3 \cos \delta],
\end{aligned}$$

$$\dot{\theta}_{23} = -\frac{Ch_\tau^2}{32\pi^2} \sin 2\theta_{23} \frac{1}{\Delta m_{31}^2} \left[c_{12}^2 |m_2 e^{i\psi_2} + m_3|^2 + s_{12}^2 \frac{|m_1 e^{i\psi_1} + m_3|^2}{1 + \xi} \right], \tag{B.1}$$

where $\Delta m_{21}^2 = m_2^2 - m_1^2$, $\Delta m_{31}^2 = m_3^2 - m_1^2$, and $\xi = \Delta m_{21}^2 / \Delta m_{31}^2$.

B.1. RGEs for the Three Phases [33]. For the Dirac phase δ ,

$$\dot{\delta} = \frac{Ch_\tau^2}{32\pi^2} \frac{\delta^{(-1)}}{\theta_{13}} + \frac{Ch_\tau^2}{8\pi^2} \delta^{(0)}, \tag{B.2}$$

where

$$\begin{aligned}
\delta^{(-1)} &= \sin 2\theta_{12} \sin 2\theta_{23} \frac{m_3}{\Delta m_{31}^2 (1 + \xi)} \\
&\times [m_1 \sin(\psi_1 - \delta) - (1 + \xi)m_2 \sin(\psi_2 - \delta) + \xi m_3 \sin \delta], \\
\delta^{(0)} &= \frac{m_1 m_2 s_{23}^2 \sin(\psi_1 - \psi_2)}{\Delta m_{21}^2} \\
&+ m_3 s_{12}^2 \left[\frac{m_1 \cos 2\theta_{23} \sin \psi_1}{\Delta m_{31}^2 (1 + \xi)} + \frac{m_2 c_{23}^2 \sin(2\delta - \psi_2)}{\Delta m_{31}^2} \right] \\
&+ m_3 c_{12}^2 \left[\frac{m_1 c_{23}^2 \sin(2\delta - \psi_1)}{\Delta m_{31}^2 (1 + \xi)} + \frac{m_2 \cos(2\theta_{23}) \sin \psi_2}{\Delta m_{31}^2} \right].
\end{aligned} \tag{B.3}$$

For the Majorana phase ψ_1 [33],

$$\begin{aligned}
\dot{\psi}_1 &= \frac{Ch_\tau^2}{8\pi^2} \left[m_3 \cos 2\theta_{23} \frac{m_1 s_{12}^2 \sin \psi_1 + (1 + \xi)m_2 c_{12}^2 \sin \psi_2}{\Delta m_{31}^2 (1 + \xi)} \right. \\
&\left. + \frac{Ch_\tau^2}{8\pi^2} \left[\frac{m_1 m_2 c_{12}^2 s_{23}^2 \sin(\psi_1 - \psi_2)}{\Delta m_{21}^2} \right] \right], \tag{B.4}
\end{aligned}$$

For the Majorana phase ψ_2 ,

$$\begin{aligned}
\dot{\psi}_2 &= \frac{Ch_\tau^2}{8\pi^2} \left[m_3 \cos 2\theta_{23} \frac{m_1 s_{12}^2 \sin \psi_1 + (1 + \xi)m_2 c_{12}^2 \sin \psi_2}{\Delta m_{31}^2 (1 + \xi)} \right] \\
&+ \frac{Ch_\tau^2}{8\pi^2} \left[\frac{m_1 m_2 s_{12}^2 s_{23}^2 \sin(\psi_1 - \psi_2)}{\Delta m_{21}^2} \right]. \tag{B.5}
\end{aligned}$$

B.2. RGEs for Neutrino Mass Eigenvalues [33].

$$\begin{aligned}
\dot{m}_1 &= \frac{1}{16\pi^2} [\alpha + Ch_\tau^2 (2s_{12}^2 s_{23}^2 + F_1)] m_1, \\
\dot{m}_2 &= \frac{1}{16\pi^2} [\alpha + Ch_\tau^2 (2c_{12}^2 s_{23}^2 + F_2)] m_2, \\
\dot{m}_3 &= \frac{1}{16\pi^2} [\alpha + 2Ch_\tau^2 c_{13}^2 c_{23}] m_3,
\end{aligned} \tag{B.6}$$

where

$$\begin{aligned} F_1 &= -s_{13} \sin 2\theta_{12} \sin 2\theta_{23} \cos \delta + 2s_{13}^2 c_{12}^2 c_{23}^2, \\ F_2 &= s_{13} \sin 2\theta_{12} \sin 2\theta_{23} \cos \delta + 2s_{13}^2 s_{12}^2 s_{23}^2. \end{aligned} \quad (\text{B.7})$$

For the MSSM case,

$$\begin{aligned} \alpha &= -\frac{6}{5} g_1^2 - 6g_2^2 + 6h_t^2, \\ C &= 1. \end{aligned} \quad (\text{B.8})$$

For the SM case,

$$\begin{aligned} \alpha &= -3g_2^2 + 2h_t^2 + 6h_b^2 + 6h_t^2 + \lambda, \\ C &= -\frac{3}{2}, \end{aligned} \quad (\text{B.9})$$

and λ is the Higgs self-coupling in the SM.

Data Availability

Data related to this work can be accessed through my zenodo doi: https://zenodo.org/records/10068005?token=eyJhbGciOiJIUzUxMiJ9.eyJpZCI6IjMwNWEzODFlTlNmQtNDazZC1hOGVmLTM3OWFlODcwZGYwMiIsImRhdGEiOnt9LCJyYW5kb20iOjJmNDhjN2QxMzU2MzgwNDQ1NWI4NDBiMzYxYjMxNGE3MiJ9.vqifuZt0X5NWkVv_UoWYmbanadokRELpk5nSA6sAp-aP5qtdNxfX0If82B3_NR M8bZMh9q-77VfcyWeRUJB2g

Conflicts of Interest

The authors declare that there is no conflict of interest regarding the publication of this paper.

Acknowledgments

One of the authors (KHD) would like to thank SCOAP³ for the financial support. This paper has previously been presented as an arXiv [34] (10.48550/arXiv.2302.11852). The editable file of this manuscript is updated on the zenodo website https://zenodo.org/records/10068005?token=eyJhbGciOiJIUzUxMiJ9.eyJpZCI6IjMwNWEzODFlTlNmQtNDazZC1hOGVmLTM3OWFlODcwZGYwMiIsImRhdGEiOnt9LCJyYW5kb20iOjJmNDhjN2QxMzU2MzgwNDQ1NWI4NDBiMzYxYjMxNGE3MiJ9.vqifuZt0X5NWkVv_UoWYmbanadokRELpk5nSA6sAp-aP5qtdNxfX0If82B3_NR M8bZMh9q-77VfcyWeRUJB2g. Here, out of 32 figures, 24 editable figure files are also given.

References

- [1] M. C. Gonzalez-Garcia, M. Maltoni, and T. Schwetz, “NuFIT: three-flavour global analyses of neutrino oscillation experiments,” *Universe*, vol. 7, no. 12, p. 459, 2021.
- [2] P. F. Harrison, D. H. Perkins, and W. G. Scott, “Tri-bimaximal mixing and the neutrino oscillation data,” *Physics Letters B*, vol. 530, no. 1-4, pp. 167–173, 2002.
- [3] K. Abe, N. Abgrall, Y. Ajima et al., “Indication of electron neutrino appearance from an accelerator produced off-axis muon neutrino beam,” *Physical Review Letters*, vol. 107, article 041801, 2011.
- [4] P. Adamson, D. J. Auty, D. S. Ayres et al., “Improved search for muon-neutrino to electron-neutrino oscillations in MINOS,” *Physical Review Letters*, vol. 107, no. 18, article 181802, 2011.
- [5] Y. Abe, C. Aberle, T. Akiri et al., “Indication of reactor $\bar{\nu}_e$ disappearance in the double Chooz experiment,” *Physical Review Letters*, vol. 108, article 131801, 2012.
- [6] F. P. An, J. Z. Bai, A. B. Balantekin et al., “Observation of electron-antineutrino disappearance at Daya Bay,” *Physical Review Letters*, vol. 108, article 171803, 2012.
- [7] J. K. Ahn, S. Chebotaryov, J. H. Choi et al., “Observation of reactor electron antineutrinos disappearance in the reno experiment,” *Physical Review Letters*, vol. 108, article 191802, 2012.
- [8] I. Gogoladze, F. Nasir, and Q. Shafi, “Non-universal Gaugino masses and natural supersymmetry,” *International Journal of Modern Physics A: Particles and Fields; Gravitation; Cosmology; Nuclear Physics*, vol. 28, no. 13, article 1350046, 2013.
- [9] J. Fan, M. Reece, and L.-T. Wang, “Precision natural SUSY at CEPC, FCC-ee, and ILC,” *Journal of High Energy Physics*, vol. 8, p. 152, 2015.
- [10] C. H. Albright and W. Rodejohann, “Comparing trimaximal mixing and its variants with deviations from tri-bimaximal mixing,” *The European Physical Journal C*, vol. 62, pp. 599–608, 2009.
- [11] X.-G. He and A. Zee, “Minimal modification to tri-bimaximal mixing,” *Physical Review D*, vol. 84, no. 5, article 053004, 2011.
- [12] K. H. Devi, K. S. Singh, and N. N. Singh, “Effects of variations of SUSY breaking scale on neutrino parameters at low energy scale under radiative corrections,” *Advances in High Energy Physics*, vol. 2022, Article ID 5780441, 17 pages, 2022.
- [13] P. H. Chankowski and Z. Pluciennik, “Renormalization group equations for seesaw neutrino masses,” *Physics Letters B*, vol. 316, no. 2-3, pp. 312–317, 1993.
- [14] K. S. Babu, C. N. Leung, and J. T. Pantaleone, “Renormalization of the neutrino mass operator,” *Physics Letters B*, vol. 319, no. 1-3, pp. 191–198, 1993.
- [15] S. Antusch, M. Drees, J. Kersten, M. Lindner, and M. Ratz, “Neutrino mass operator renormalization revisited,” *Physics Letters B*, vol. 519, no. 3-4, pp. 238–242, 2001.
- [16] S. Antusch, J. Kersten, M. Lindner, M. Ratz, and M. A. Schmidt, “Running neutrino mass parameters in see-saw scenarios,” *Journal of High Energy Physics*, vol. 2005, no. 3, p. 024, 2005.
- [17] M. Chala and A. Titov, “Neutrino masses in the standard model effective field theory,” *Physical Review D*, vol. 104, no. 3, article 035002, 2021.
- [18] K. S. Singh and N. N. Singh, “Effects of the variation of SUSY breaking scale on Yukawa and gauge couplings unification,” *Advances in High Energy Physics*, vol. 2015, Article ID 652029, 8 pages, 2015.
- [19] K. S. Singh, S. Roy, and N. N. Singh, “Stability of neutrino parameters and self-complementarity relation with varying SUSY breaking scale,” *Physical Review D*, vol. 97, no. 5, article 055038, 2018.
- [20] S. K. Kang and C. S. Kim, “Prediction of leptonic CP phase from perturbatively modified tribimaximal (or bimaximal) mixing,” *Physical Review D*, vol. 90, no. 7, article 077301, 2014.

- [21] W. Rodejohann, H. Zhang, and S. Zhou, “Systematic search for successful lepton mixing patterns with nonzero θ_{13} ,” *Nuclear Physics B*, vol. 855, pp. 592–607, 2012.
- [22] S. K. Garg, “Model independent analysis of Dirac CP violating phase for some well-known mixing scenarios,” *International Journal of Modern Physics A*, vol. 36, no. 18, article 2150118, 2021.
- [23] S.-P. Li, Y. Y. Li, X.-S. Yan, and X. Zhang, “Next-to-tribimaximal mixing against CP violation and baryon asymmetry signs,” *Physical Review D*, vol. 105, no. 9, 2022.
- [24] V. D. Barger, M. S. Berger, and P. Ohmann, “Supersymmetric grand unified theories: two-loop evolution of gauge and Yukawa couplings,” *Physics Letters B*, vol. 47, no. 3, pp. 1093–1113, 1993.
- [25] D. R. T. Jones and L. Mezincescu, “The β -function in supersymmetric Yang-Mills theory,” *Physics Letters B*, vol. 136, no. 4, pp. 242–244, 1984.
- [26] PD Group, R. L. Workman, V. D. Burkert et al., “Review of particle physics,” *Progress of Theoretical and Experimental Physics*, vol. 2022, no. 8, article 083C01, 2022.
- [27] P. F. de Salas, D. V. Forero, S. Gariazzo et al., “2020 global reassessment of the neutrino oscillation picture,” *Journal of High Energy Physics*, vol. 71, no. 2, 2021.
- [28] J. E. Bjorkman and D. R. T. Jones, “The unification mass, $n^2\theta_W$ and M_b/M_τ in nonminimal supersymmetric SU(5),” *Nuclear Physics B*, vol. 259, p. 533, 1985.
- [29] M. Patgiri and N. N. Singh, “New uncertainties in QCD-QED rescaling factors using quadrature method,” *Pramana*, vol. 65, pp. 1015–1025, 2006.
- [30] S. Alam, M. Aubert, S. Avila et al., “Completed SDSS-IV extended baryon oscillation spectroscopic survey: cosmological implications from two decades of spectroscopic surveys at the Apache Point Observatory,” *Physical Review D*, vol. 103, no. 8, article 083533, 2021.
- [31] N. Aghanim, Y. Akrami, M. Ashdown et al., “Planck 2018 results. VI. Cosmological parameters,” *Astronomy & Astrophysics*, vol. 641, p. A6, 2020.
- [32] A. Sirunyan, A. Tumasyan, W. Adam et al., “A measurement of the Higgs boson mass in the diphoton decay channel,” *Physics Letters B*, vol. 805, article 135425, 2020.
- [33] S. Antusch, J. Kersten, M. Lindner, and M. Ratz, “Running neutrino masses, mixings and CP phases: analytical results and phenomenological consequences,” *Nuclear Physics B*, vol. 674, no. 1-2, pp. 401–433, 2003.
- [34] K. H. Devi, K. S. Singh, and N. N. Singh, “Stability of the next-to-tribimaximal mixings under radiative corrections with the variation of SUSY breaking scale in MSSM,” 2023, <https://arxiv.org/abs/2302.11852>.